Supplementary Information (SI) for Inorganic Chemistry Frontiers.
This journal is © the Partner Organisations 2024

Supporting information

Constructing Ni Species-Incorporated CoP@N-Doped Carbon Nanosheet Arrays for Efficient Self-Powered Hydrazine-Assisted Seawater Electrolysis

Feng-Xiao Yan, Hao-Yu Wang, Lei Wang, Hao Wang, Zhong-Yong Yuan*

School of Materials Science and Engineering, Smart Sensing Interdisciplinary Science Center, Nankai University, Tianjin 300350, China

* Corresponding author. *E-mail address*: zyyuan@nankai.edu.cn

1. Experimental section

1.1 Materials

Ammonium chloride (NH_4Cl, 99.5%), potassium hydroxide (KOH, 85%) were received from Tianjin Bohua Chemical Reagent Co., Ltd. 2-methylimidazole was obtained from Shanghai Merrier Biochemical Technology Co., Ltd. Cobaltous nitrate ($Co(NO_3)_2 \cdot 6H_2O$, 99.9%) was obtained from Shanghai Titan Technology Co., Ltd, Nickel nitrate ($Ni(NO_3)_2 \cdot 6H_2O$, 98.0%) was obtained from Tianjin Damao Chemical Regent Factory. Chloride hexahydrate ($CoCl_2 \cdot 6H_2O$, 99.0%) was purchased from Tianjin Fengchuan Chemical Reagent Technology Co., Ltd. Sodium hypophosphite ($NaH_2PO_2 \cdot H_2O$, 99.0%) and acetone (99.5%) were ordered from Tianjin Chemical Reagent Supply and Marketing Co., Ltd. Nickel foam (99%) used in the study was obtained from Shanxi Lizhiyuan Technology Co., Ltd. Ethanol (99.7%) was received from Concord Technology Co., Ltd. Hydrochloric acid (HCl, 36.0% ~ 38.0%) was purchased from Yongfei Chemical Reagent Co., Ltd. Deionized water was obtained from Tianjin Huaxun Medical Technology Co., Ltd. Moreover, 20 wt% Pt/C was received from Shanghai Hesen Electric Co., Ltd. Hydrazine hydrate ($N_2H_4 \cdot H_2O$, 80%) was purchased from Tianjin Damao Chemical Reagent Co., Ltd.

1.2 Electrochemical measurements

Electrochemical characterization was conducted using a CHI 760E electrochemical station in alkaline electrolyte at room temperature. A typical three-electrode setup was employed, comprising the prepared sample as the working electrode, a platinum wire as the counter electrode and a Hg/HgO electrode reference. This setup facilitated the assessment of electrocatalytic performance for HER, OER and HzOR. Moreover, seawater splitting electrolysis and hydrazine-assisted seawater splitting were carried out in a two-electrode configuration, utilizing Ni-CoP@NC material as both the anode and cathode. The experiments were conducted in different electrolytes: 1.0 M KOH and 1.0 M KOH with 0.2 M hydrazine, respectively. Besides, Electrocatalytic methanol oxidation, ethanol oxidation, glucose oxidation, and urea oxidation were conducted in different electrolytes: 0.1 M methanol solution, ethanol solution, glucose solution and

urea solution, respectively.

In this study, all potentials were referenced to the reversible hydrogen electrode (RHE) using the formula: $E_{vs\ RHE} = E_{vs\ Hg/HgO} + 0.059\ pH + E_{vs\ Hg/HgO}$. The working electrodes had a geometric surface area of approximately 0.5 cm^{-2}. Linear sweep voltammetry (LSV) was conducted at a scan rate of 5 mV s^{-1}, with the Tafel slope was determined using the Tafel equation ($\eta = a + b\log j$). The double layer capacitance (C_{dl}) was calculated from cyclic voltammetry (CV) data obtained at scan rates ranging from 10 to 30 mV s^{-1} using the equation $C_{dl} = (j_a - j_c)/(2*\nu)$.

Electrochemical impedance spectroscopy (EIS) was conducted across a frequency range of 0.01 to 100000 Hz with an amplitude of 5 mV. Stability tests for HER and HzOR were performed over 24 hours in both 1 M KOH and 1 M KOH with 0.5 M N_2H_4. Similarly, the stability of hydrazine-assisted seawater splitting was assessed in natural seawater with 0.5 M N_2H_4 at a constant current density of 200 mA cm^{-2} over 48 hours.

The fuel cell was assembled using Ni-CoP@NC as anode and Ni foam-supported commercial Pt/C catalyst as cathode. The anode was immersed in 1 M KOH with 0.2 M N_2H_4, while cathodic electrolyte was 1 M KOH. The Zn-Hz battery was assembled using Ni-CoP@NC as cathode and Zn foil as anode, separated by anion exchange membrane (AEM) as separator. The cathode was immersed in 1 M KOH with 0.2 M N_2H_4, while anodic electrolyte was 1 m KOH with 0.02 M $Zn(CH_3COO)_2$.

1.3 Techno-economic analysis

Energy consumption (EC) (kWh Kg^{-1} H_2) was calculated according to the following equation: Energy consumption (EC) (kWh Kg^{-1} H_2) is calculated according to the following equation:

$$EC = UIt/1000$$

$$Q = nZF = It$$

where, U is the cell voltage, and the cell voltage is calculated on the assumption that the required anodic potential is 1.23 V vs. RHE without overpotentials; I is the current; t represents the time to remove 1 kg H_2; Q is the actual consumed charge amount; F is the

faradaic constant (96485 C mol^{-1}); *z* is the number of transferred electrons (*n* = 2); and n is the amount of H_2 in mol (1 kg H_2 = 500 mol). And then, the cost for producing per kg H_2 was calculated he electricity cost of \$0.104 per kWh in China.

1.4 Density functional theory

To investigate the electroactivity, DFT calculations have been applied to reveal the electronic modulations induced by Ni species-incorporated Co_2P nanosheet arrays encapsulated in N-doped carbon layers grown on Ni foam. To accurately describe the exchange-correlation interactions, we have selected the generalized gradient approximation (GGA) and Perdew-Burke-Ernzerhof (PBE) functionals. Meanwhile, the plane-wave basis cutoff energy has been set to 450 eV based on the ultrafine quality and the ultrasoft pseudopotentials. The Broyden-Fletcher-Goldfarb-Shannon (BFGS) algorithm is selected for all the geometry optimizations. The coarse quality of k points has been applied for all the energy minimizations. We have selected the (121) surfaces of Co_2P as a representative surface to investigate the electronic modulation induced by Ni incorporating, which is consistent with the experimental characterizations. To guarantee sufficient relaxation, we have introduced 15 Å vacuum space on the z-axis. To achieve convincing convergence, the following criteria are applied for all the geometry optimizations including the Hellmann-Feynman forces should not exceed 0.001 eV/Å; the total energy difference should not be over 5×10^{-5} eV/atom, and the inter-ionic displacement should be less than 0.005 Å.

The oxidation of hydrazine into nitrogen and hydrogen occurs in the following six consecutive elementary steps:

$$(A)\ * + N_2H_4 \rightarrow *N_2H_4, \quad (1)$$

$$(B)\ *N_2H_4 \rightarrow *N_2H_3 + H^+ + e^-, \quad (2)$$

$$(C)\ *N_2H_3 \rightarrow *N_2H_2 + H^+ + e^-, \quad (3)$$

$$(D)\ *N_2H_2 \rightarrow *N_2H + H^+ + e^-, \quad (4)$$

$$(E)\ *N_2H \rightarrow *N_2 + H^+ + e^-, \quad (5)$$

$$(F)\ *N_2 \rightarrow * + N_2. \quad (6)$$

The asterisk (*) represents the reaction surfaces. "$*N_2H_4$", "$*N_2H_3$", "$*N_2H_2$", "$*N_2H$",

and "*N_2" denote the models with the corresponding chemisorbed species residing in the reaction surfaces. Among these six elementary steps, steps (A) and (F) are the adsorption of N_2H_4 and desorption of N_2, respectively. The other four elementary steps involve the generation of one proton and one electron. Then, using the computational hydrogen electrode (pH = 0, P = 1 atm, T = 298 K), the Gibbs free energy of $H^+ + e^-$ was replaced implicitly with the Gibbs free energy of one-half an H_2 molecule. Thus the reaction Gibbs free energies can be calculated with Eqs:

$$\triangle G_A = \triangle G_{*N2H4} - \triangle G_* - \triangle G_{N2H4} \quad (7)$$

$$\triangle G_B = \triangle G_{*N2H3} + 0.5\triangle G_{H2} - \triangle G_{*N2H4} - eU - kTIn10*pH \quad (8)$$

$$\triangle G_C = \triangle G_{*N2H2} + 0.5\triangle G_{H2} - \triangle G^*_{N2H3} - eU - kTIn10*pH \quad (9)$$

$$\triangle G_D = \triangle G_{*N2H} + 0.5\triangle G_{H2} - \triangle G_{*N2H2} - eU - kTIn10*pH \quad (10)$$

$$\triangle G_E = \triangle G_{*N2} + 0.5\triangle G_{H2} - \triangle G_{*N2H} - eU - kTIn10*pH \quad (11)$$

$$\triangle G_F = \triangle G_* + G_{N2} - \triangle G_{*N2} \quad (12)$$

U and the pH value in this work is set to zero. The adsorption or reaction Gibbs free energy is defined as $\triangle G = \triangle E + (ZPE - T\triangle S)$, where ΔE is the adsorption or reaction energy based on DFT calculations, ΔZPE is the zero-point energy (ZPE) correction, T is the temperature, and ΔS is the entropy change. For each system, its ZPE can be calculated by summing vibrational frequencies overall normal modes ν (ZPE = 1/2 Σħν). The entropies of gas-phase H_2, N_2, and NH_2NH_2 are obtained from the NIST database[3] with the standard condition, and the adsorbed species were only taken vibrational entropy (S_v) into account, as shown in the following formula:

$$S_v = \Sigma i\, R\{h\nu_i/[k_BT * \exp(h\nu_i/k_BT) - k_BT] - In[1 - \exp(-h\nu_i/k_BT)]\} \quad (13)$$

Among which R = 8.314 J·mol^{-1}·K^{-1}, T = 298.15 K, h = 6.63 ×10^{-34} J·s, k_B = 1.38 × 10^{-23} J·K^{-1}, i is the frequency number, ν_i is the vibrational frequency (unit is cm^{-1}).

Under the standard condition, the overall HER pathway includes two steps: first, adsorption of hydrogen on the catalytic site (*) from the initial state ($H^+ + e^- + *$), second, release the product hydrogen (1/2 H_2). The total energies of $H^+ + e^-$ and 1/2 H_2

are equal. Therefore, the Gibbs free energy of the adsorption of the intermediate hydrogen on a catalyst (ΔG_H) is the key descriptor of the HER activity of the catalyst and is obtained by:

$$\Delta G_H = \Delta E_H + \Delta ZPE - T\Delta S$$

where ΔE_H, ΔZPE and ΔS are the adsorption energy, zero-point energy change and entropy change of H adsorption, respectively.

2. Supplementary figures

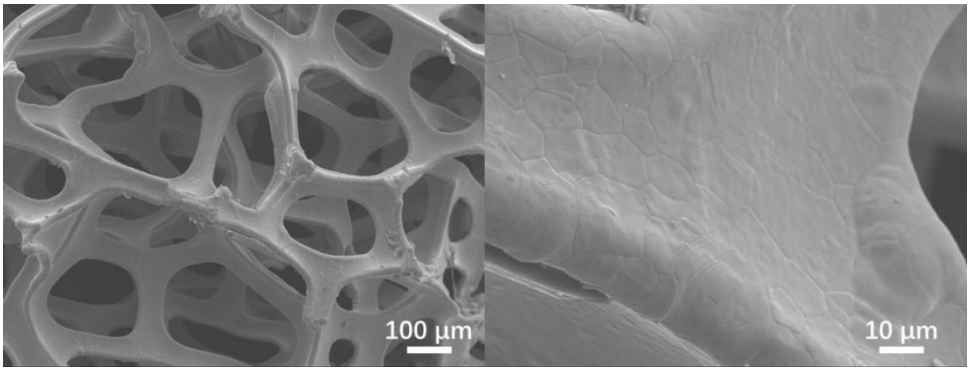

Fig. S1. SEM images of original Ni foam (NF).

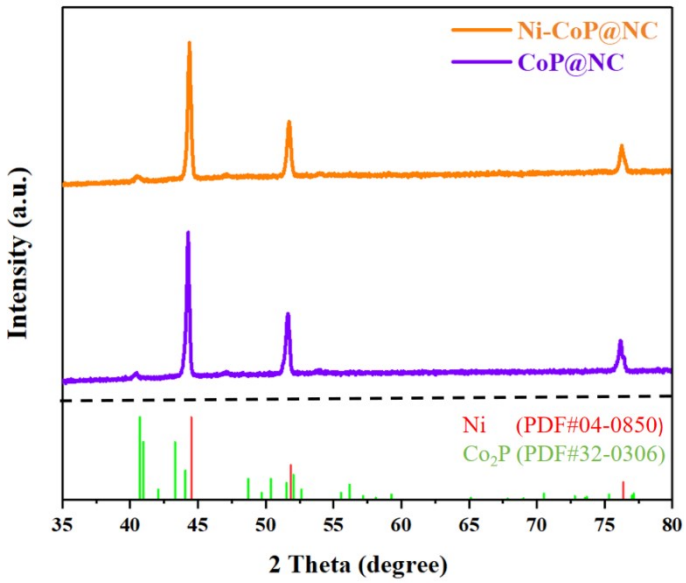

Fig. S2. Magnified XRD patterns of Ni-CoP@NC and CoP@NC.

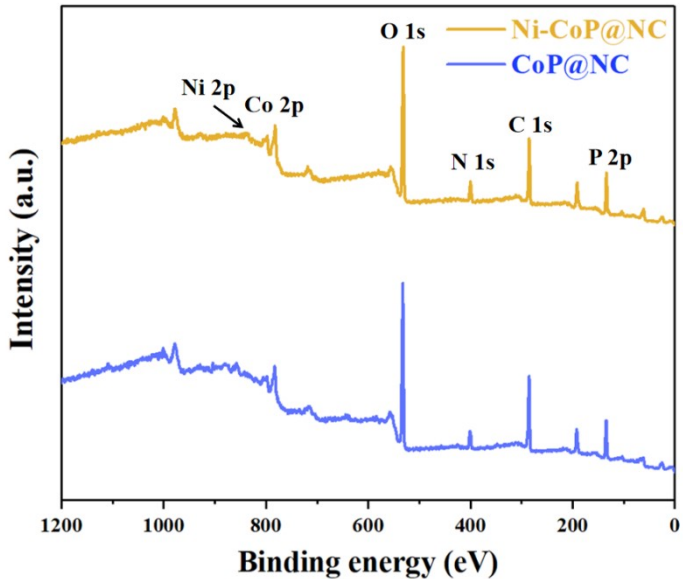

Fig. S3. XPS survey spectra for Ni-CoP@NC and CoP@NC.

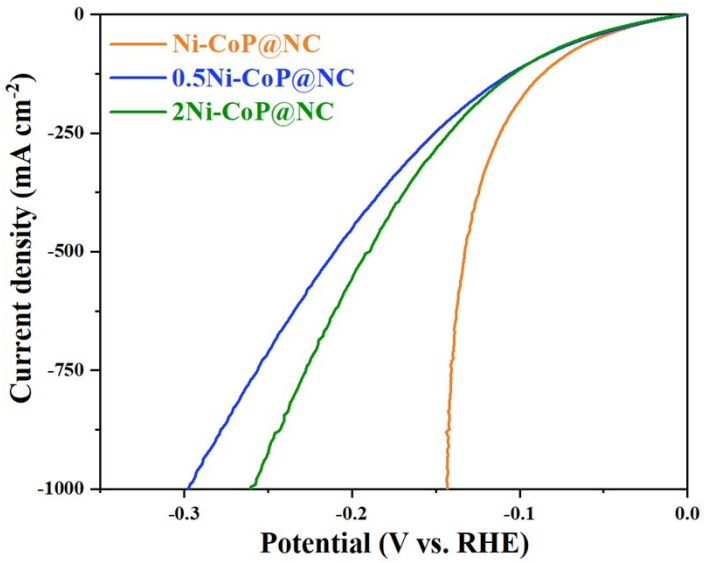

Fig. S4. LSV curves of samples with different Ni species incorporating.

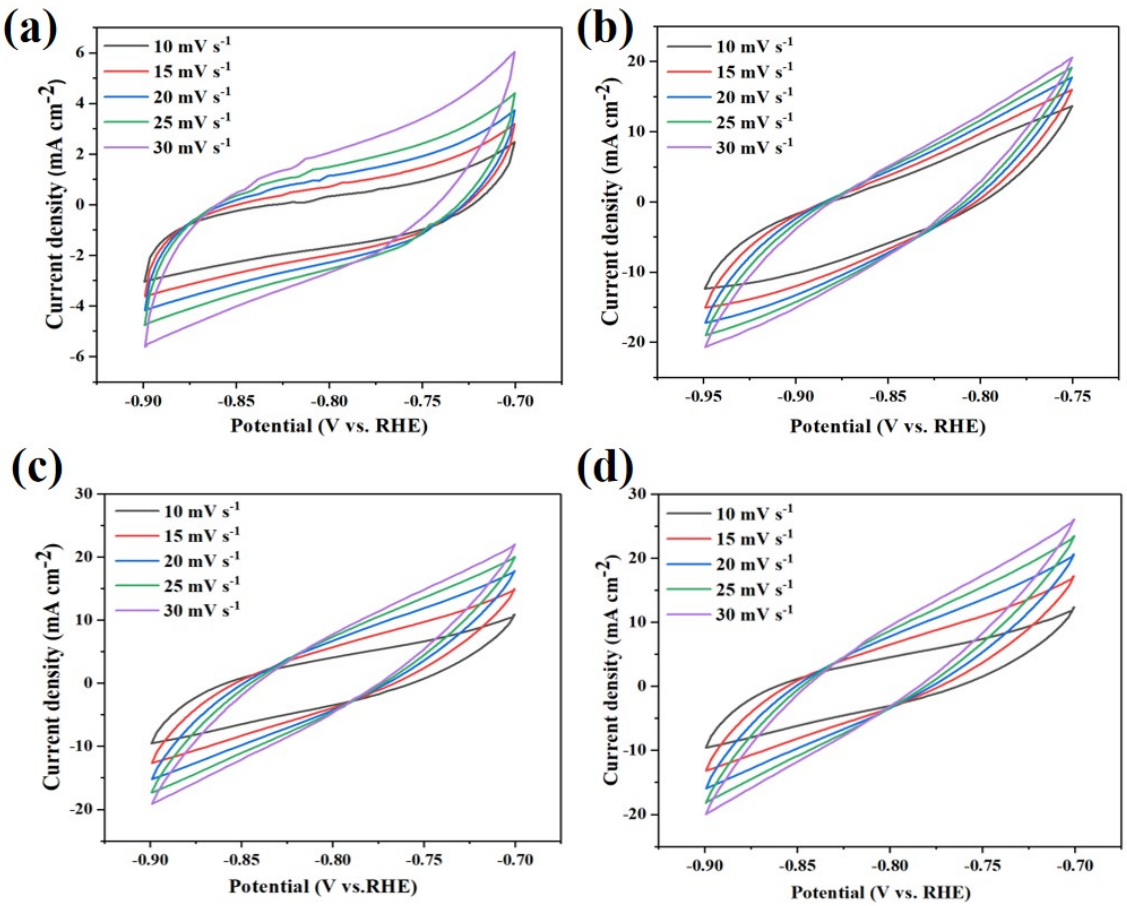

Fig. S5. CVs with different scan rates from 30 mV s^{-1} to 10 mV s^{-1} of (a) Ni-CoP@NC, (b) CoP@NC, (c) 0.5Ni-CoP@NC and (d) 2Ni-CoP@NC.

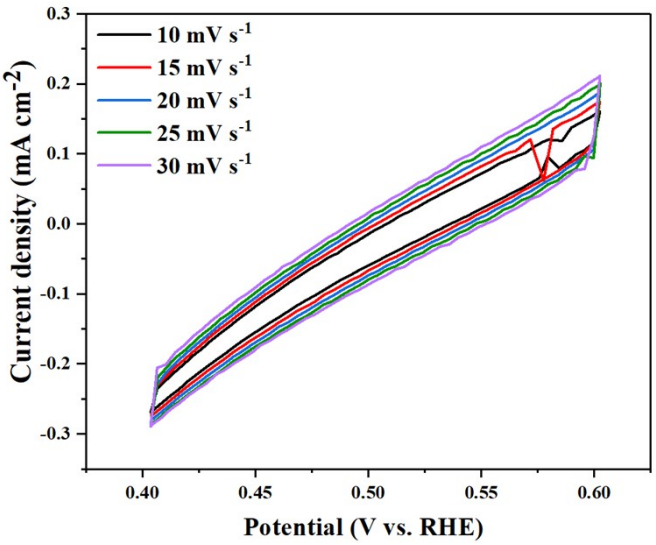

Fig. S6. CVs with different scan rates from 30 mV s^{-1} to 10 mV s^{-1} of NF.

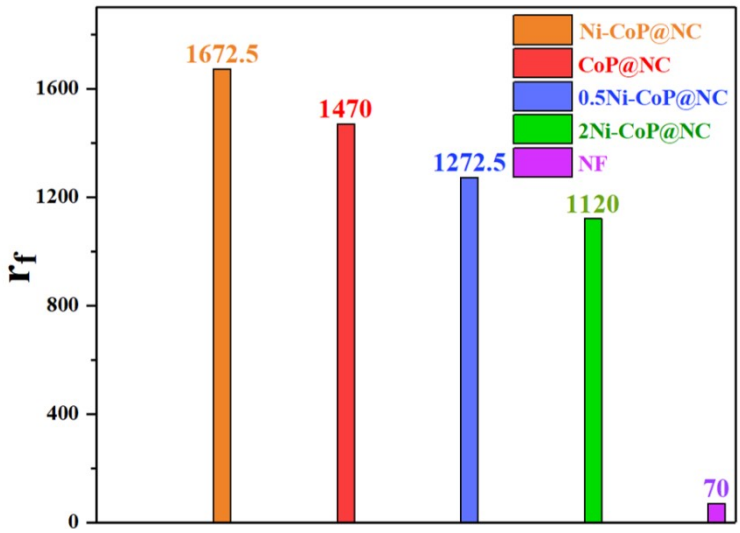

Fig. S7. Roughness factor of Ni-CoP@NC, CoP@NC, 0.5Ni-CoP@NC, 2Ni-CoP@NC and NF.

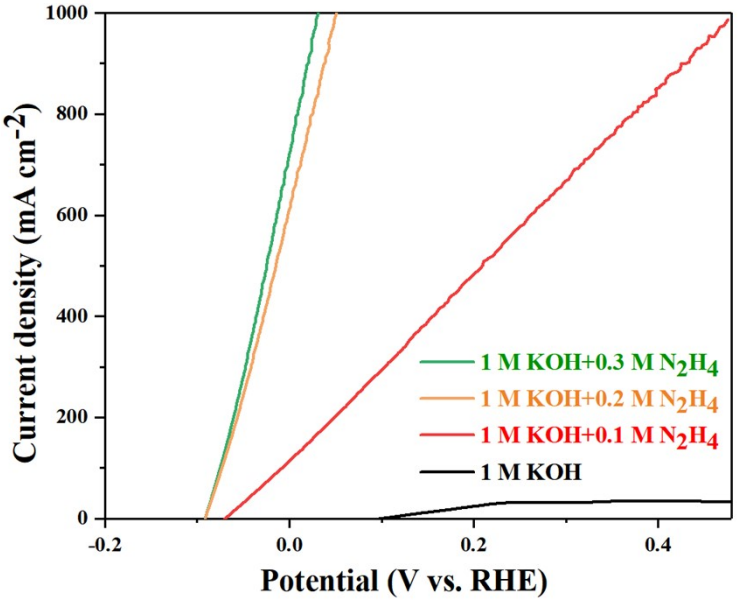

Fig. S8. LSV curves of Ni-CoP@NC in 1.0 M KOH with various hydrazine concentrations.

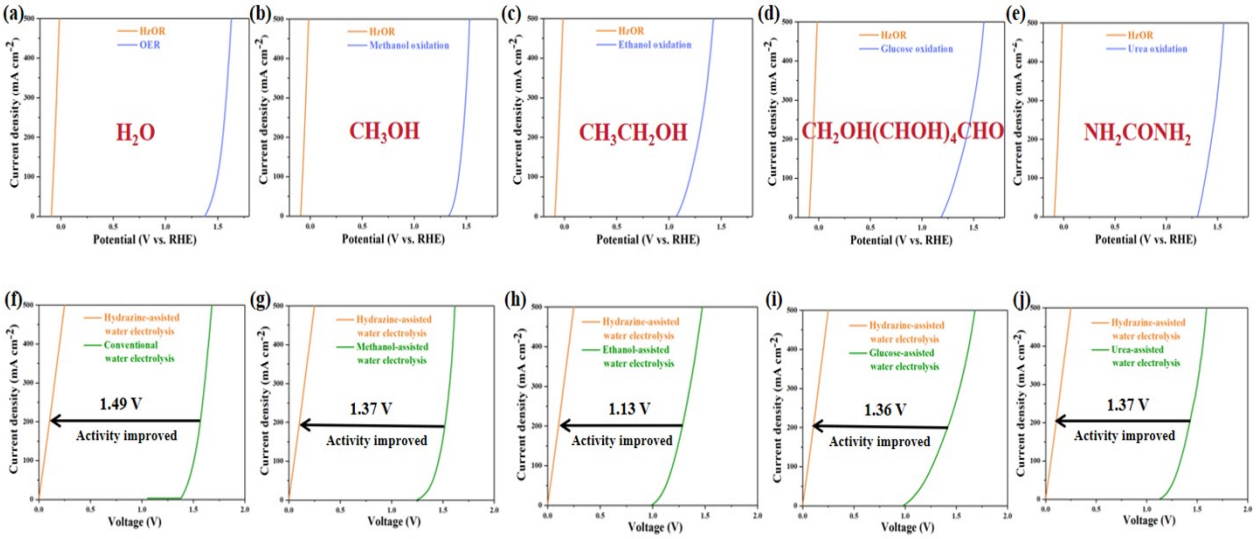

Fig. S9. The electrocatalytic process of Ni-CoP@NC across various reactions including (a) electrocatalytic oxygen evolution, (b) methanol oxidation, (c) ethanol oxidation, (d) glucose oxidation, and (e) urea oxidation. Employing Ni-CoP@NC in (f) conventional water electrolysis system, (g) methanol-assisted water electrolysis system, (h) ethanol-assisted water electrolysis system, (i) glucose-assisted water electrolysis system, and (j) urea-assisted water electrolysis system.

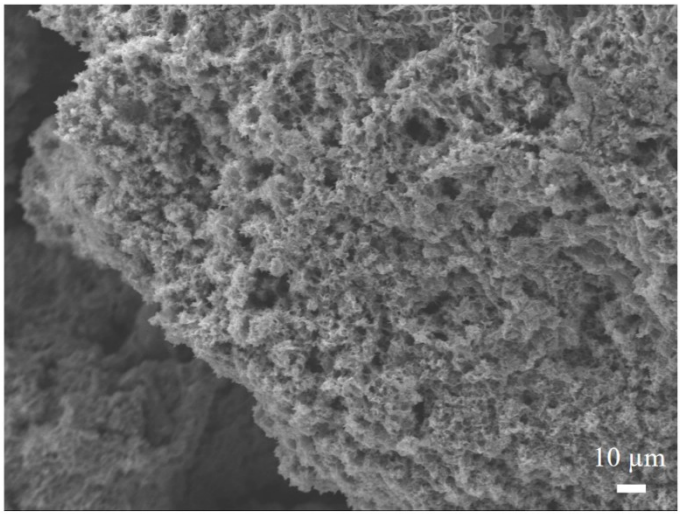

Fig. S10. SEM image of the post-HER Ni-CoP@NC.

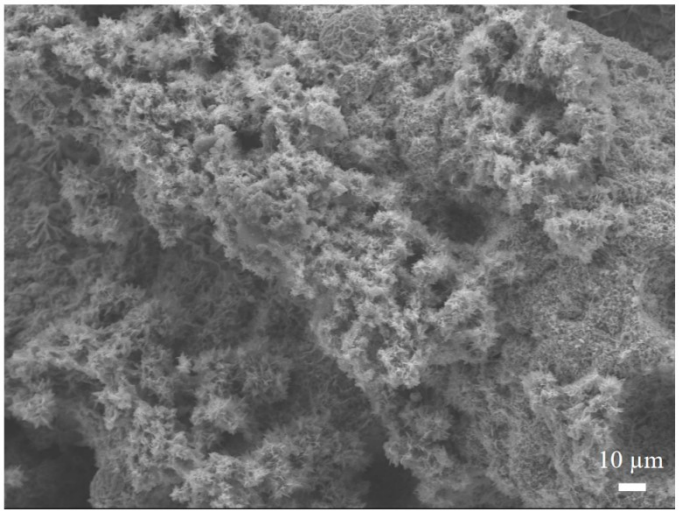

Fig. S11. SEM image of the post-HzOR Ni-CoP@NC.

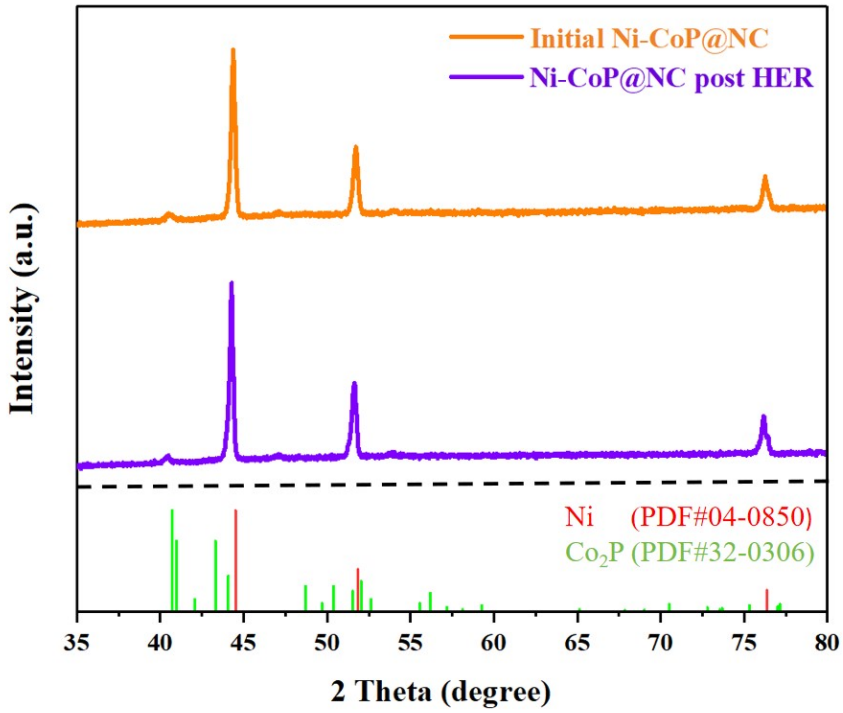

Fig. S12. XRD characterization of initial Ni-CoP@NC and Ni-CoP@NC after long-term HER ability measurements.

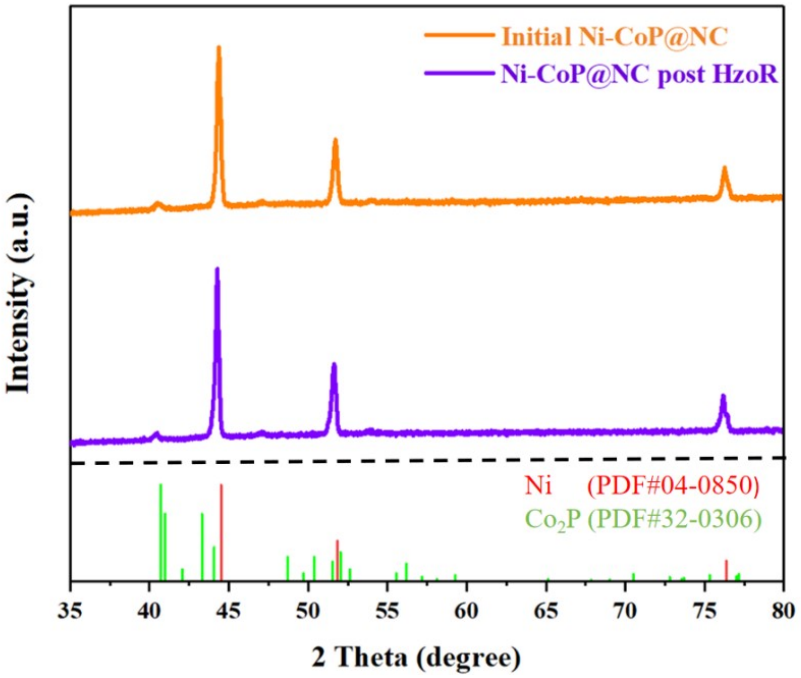

Fig. S13. XRD characterization of initial Ni-CoP@NC and Ni-CoP@NC after long-term HzOR ability measurements.

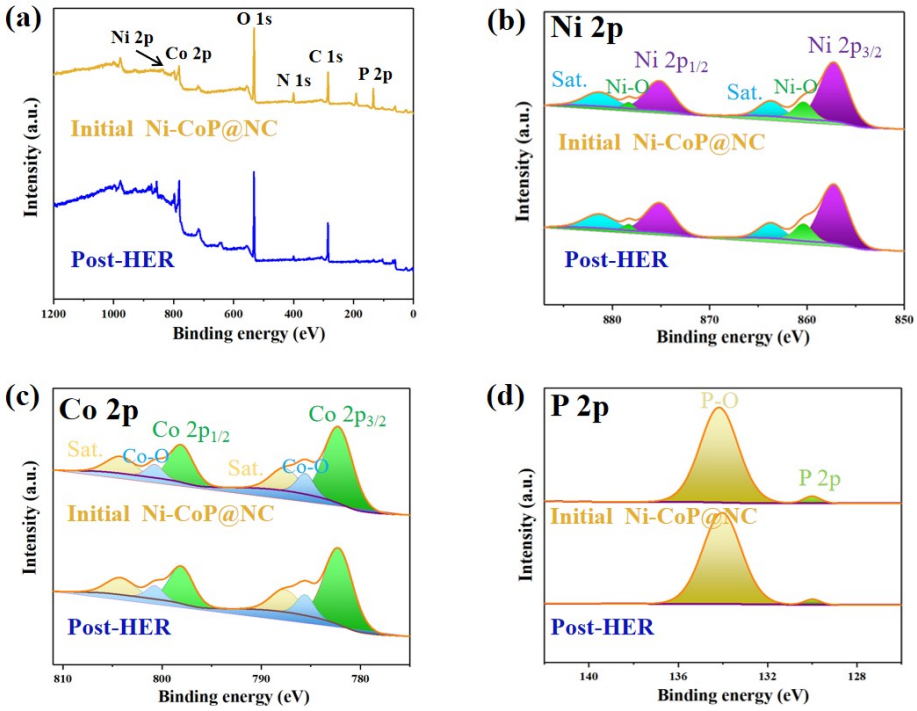

Fig. S14. XPS characterization of initial Ni-CoP@NC and Ni-CoP@NC after long-term HER ability measurements: (a) survey, (b) Ni 2p, (c) Co 2p and (d) P 2p spectra.

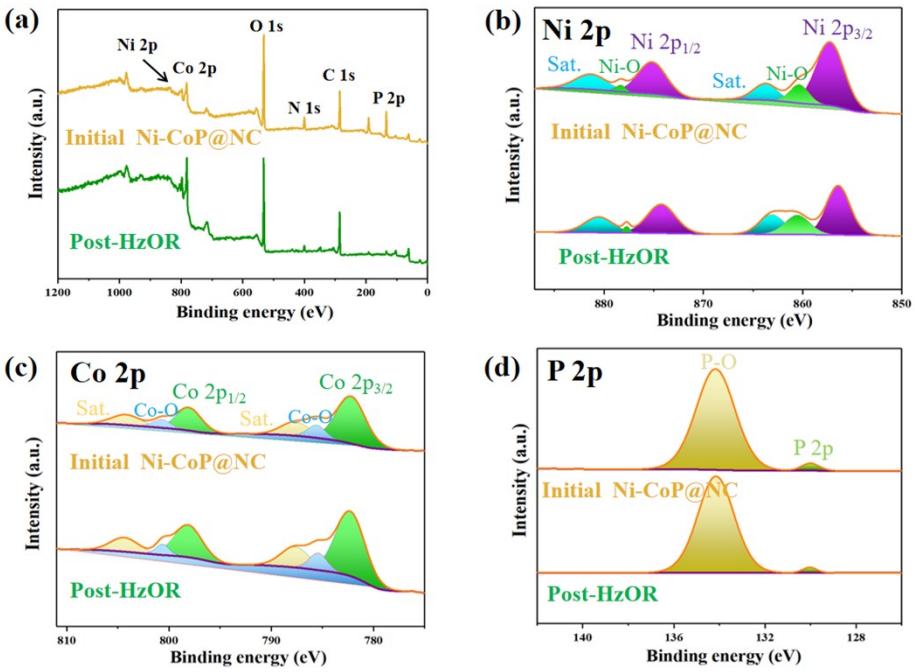

Fig. S15. XPS characterization of initial Ni-CoP@NC and Ni-CoP@NC after long-term HzOR ability measurements: (a) survey, (b) Ni 2p, (c) Co 2p and (d) P 2p spectra.

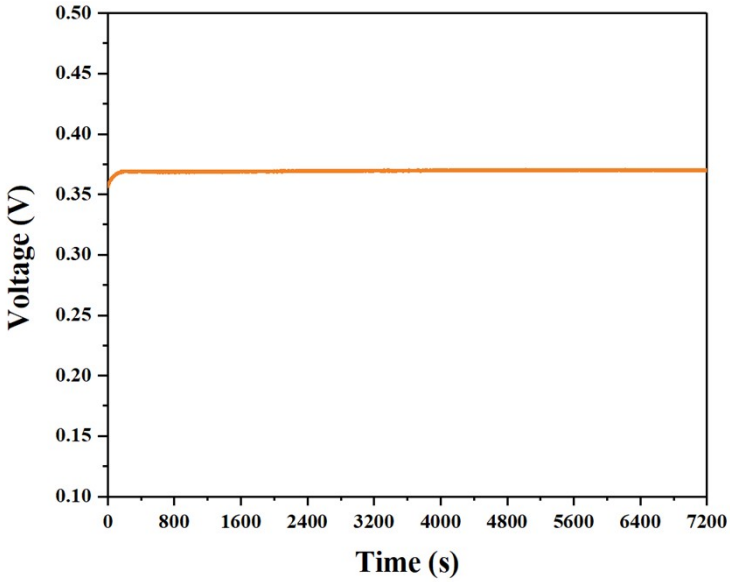

Fig. S16. Open circuit voltages of Ni-CoP@NC assembled Zn-hydrazine battery.

3. Supplementary tables

Table S1. Comparison of HER performance of Ni-CoP@NC with other electrocatalysts.

Catalyst	Electrolyte	Overpotential at 1000 mA cm^{-2} (mV)	Reference
Ni-CoP@NC	1.0 M KOH	143	This work
MIL-(IrNiFe)@NF	1.0 M KOH	198	[1]
FeNi LDH@FF	1.0 M KOH	400	[2]
Ru-CoO_x/NF	1.0 M KOH	252	[3]
Ir-nc@m-NiCo	1.0 M KOH	146	[4]
NiMo/Mo_2N/NC(500)	1.0 M KOH	271	[5]
MoWNiTe	1.0 M KOH	182	[6]
MoO_2/@Ru NT	1.0 M KOH	131	[7]
DE 150s ribbon	1.0 M KOH	104	[8]
RuGa/N-rGO-2	1.0 M KOH	156	[9]
Ni-MoN-450	1.0 M KOH	190	[10]
Co-SA/CC	1.0 M KOH	300	[11]
MnCo/NiSe	1.0 M KOH	211	[12]
$MnCo_2S_4$@MoS_2/NF	6.0 M KOH	208	[13]
$SnFeS_xO_y$/NF	1.0 M KOH	324	[14]
Cu_2S@NiS@Ni/NiMo	1.0 M NaOH + 0.5 M NaCl	200	[15]

Table S2. Comparison of HzOR performance of Ni-CoP@NC with other electrocatalysts.

Catalyst	Electrolyte	Potential at 1000 mA cm^{-2} (mV)	Reference
Ni-CoP@NC	1.0 M KOH + 0.2 M N_2H_4	51	This work
Ni_2Fe_2N/NF	alkaline hydrazine solution	300	[16]
Ru-FeP_4/IF	1.0 M KOH + seawater + 0.5 M N_2H_4	335	[17]
a-Ni_xP/Ni/NF	1.0 M NaOH + 0.5 M N_2H_4	240	[18]
Ru-Cu_2O/CF	1.0 M NaOH + 0.5 M N_2H_4	135	[19]
CoP/CF	1.0 M NaOH + 0.4 M N_2H_4	180	[20]
Fe-Ni_2P@MIL-FeNi	1.0 M KOH + 0.5 M N_2H_4 seawater	200	[21]
MoNi@NF	1.0 M KOH + 0.5 M N_2H_4 seawater	470	[22]
FeNiP-NPHC	1.0 M KOH + 0.5 M N_2H_4 seawater	110	[23]
RuFe-Ni_2P@NF	1.0 M KOH + Seawater + 0.5 M N_2H_4	260	[24]
CoP/Ni_2P@NF	1 M KOH + 0.5 M N_2H_4 seawater.	110	[25]
CoH-CoPV@CFP	1.0 M KOH + 0.4 M N_2H_4	117	[26]

Table S3. Comparison of OHzS performance of Ni-CoP@NC with other electrocatalysts.

Catalyst	Electrolyte	Potential at 1000 mA cm^{-2} (V)	Reference
Ni-CoP@NC	1.0 M KOH + 0.5 M N_2H_4	0.49	This work
NiMo/Ni_2P	1.0 M KOH + 0.5 M N_2H_4	0.21	[27]
FeNiP-NPHC	1.0 M KOH + 0.5 M N_2H_4	0.51	[23]
Fe-CoNiP@NC	1.0 M KOH + 0.5 M N_2H_4	0.56	[28]
F-CoP/CF	1.0 M KOH + 0.2 M N_2H_4	0.49	[20]
RuFe-Ni_2P@NF	1.0 M KOH + 0.5 M N_2H_4	0.70	[29]
FeCo-Ni_2P@MIL-FeCoNi	1.0 M KOH + 0.5 M N_2H_4	0.40	[21]
Ru-FeP_4/IF	1.0 M KOH + 0.5 M N_2H_4	0.90	[17]
Mo-Ni_2P_v@MNF	1.0 M KOH+0.5 M N_2H_4	0.57	[30]
MoNi@NF	1.0 M KOH + 0.5 M N_2H_4	0.54	[22]
Fe/F-Ni_2P@NC	1.0 M KOH + 0.5 M N_2H_4	0.57	[24]

Table S4. Comparison of OWS performance of Ni-CoP@NC with other electrocatalysts.

Catalyst	Electrolyte	Potential at 1000 mA cm^{-2} (V)	Reference
Ni-CoP@NC	1.0 M KOH	1.82	This work
$Co_{0.03}$-$NiFe_{0.97}$LDH	1.0 M KOH	1.53	[31]
Ir/$CoMoO_4$/NF	1.0 M KOH	1.81	[32]
$MnCo_2S_4$@MoS_2/NF	6.0 M KOH	1.79	[33]
LVN-0.1	1.0 M KOH	1.94	[34]
FeOOH/Co_9S_8/Ni_3S_2	1.0 M KOH	1.80	[35]
nano-KFO/NF	1.0 M KOH	1.95	[36]
CoB@MOF@CC	1.0 M KOH	2.10	[37]
NiO/RuO_2/NF	6.0 M KOH	1.78	[38]

References

[1] X.-J. Zhai, Q.-P. Yu, G.-S. Liu, J.-L. Bi,Y. Zhang, J.-Q. Chi, J.-P. Lai, B. Yang, L. Wang, Hierarchical microsphere MOF arrays with ultralow Ir doping for efficient hydrogen evolution coupled with hydrazine oxidation in seawater, *J. Mater. Chem. A*, 2021, **9**, 27424-27433.

[2] Y. Feng, Y. Wei, S.-J. Liu, P. Li, K. Akhtar, E.-M. Bakhsh, S.-B. Khan, Y. Shen, Enhanced hydrogen evolution reaction activity of FeNi layered double hydroxide modified with Ruthenium nanoparticles at high current density, *J. Electroanal.*, 2023, **938**, 117451.

[3] T. Wu, M.-Z. Sun, H.-H. Wong, C.-H. Chan, L. Lu, Q.-Y. Lu, B.-A. Chen, B.-L. Huang, Recent advances and strategies of electrocatalysts for large current density industrial hydrogen evolution reaction, *Inorg. Chem. Front.*, 2023, **10**, 4632-4649.

[4] J.-X. Yuan, J.-S. Zhou, Z.-H. Peng, G. Li, Y. Hou, K.-H. Leung, Enhanced electrocatalytic hydrogen evolution in alkaline saline electrolyte by NiCo foam supported iridium nanoclusters, *J. Mater. Chem. A*, 2024, **12**, 2383-2390.

[5] H.-L. Jia, H.-Y. Wang, F.-F. Yan, H.-C. Zhang, Z. Li, J.-J. Wang, Unravelling electrocatalytic concerted diatomic-ensembles over superior hydrogen-evolution array structured by NiMo/Mo_2N heteronanojunctions, *Appl. Catal. B-Environ.*, 2024, **343**, 123362.

[6] S.-H. Jo, W.-X. Liu, Y.-A. Yue, K.-H. Shin, K.-B. Lee, H. Choi, B. Hou, J. Sohn, Novel ternary metals-based telluride electrocatalyst with synergistic effects of high valence non-3d metal and oxophilic Te for pH-universal hydrogen evolution reaction, *J. Energy Chem.*, 2023, **80**, 736-743.

[7] Y. Zhang, C.-Q. Ma, X.-J. Zhu, K.-Y. Qu, P.-D. Shi, L.-Y. Song, J. Wang, Q.-P. Lu, A.-L. Wang, Hetero-Interface Manipulation in MoO_x@Ru to Evoke Industrial Hydrogen Production Performance with Current Density of 4000 mA cm^{-2}, *Adv. Energy Mater.*, 2023, **13**, 2301492.

[8] X.-Y. Zhang, Y.-Y. Yang, Y.-J. Liu, Z. Jia, Q.-Q. Wang, L.-G. Sun, L.-C. Zhang, J.-J. Kruzic, J. Lu, B.-L. Shen, Defect Engineering of a High-Entropy Metallic Glass

Surface for High-Performance Overall Water Splitting at Ampere-Level Current Densities, *Adv. Mater.*, 2023, **35**, 2303439.

[9] H.-F. Zhang, C.-Q. Cheng, J. Zhou, C.-Q. Ma, P.-D. Shi, H.-M. Wu, P.-F. Yin, W.-B. Cao, J. Xia, L.-J. Zhu, A.-L. Wang, Q.-P. Lu, Atomically dispersed ruthenium sites with electron-rich environments in intermetallic compounds for high-current-density hydrogen evolution, *J. Mater. Chem. A*, 2023, **11**, 10328-10336.

[10] Y.-B. Liu, B.-W. Zhou, Y.-B. Zhang, W.-P. Xiao, B. Li, Z.-X. Wu, L. Wang, In situ synthesis of two-dimensional graphene-like nickel-molybdenum nitride as efficient electrocatalyst towards water-splitting under large-current density, *J. Colloid Interface Sci.*, 2023, **637**, 104-111.

[11] P.-W. Zhao, C. Peng, Q.-C. Zhang, X.-B. Fan, H.-Y. Chen, Y.-Z. Zhu, Y. Min, Carbon-coordinated atomic cobalt directly embedded on carbon cloth for alkaline hydrogen evolution at high current density, *Chem. Eng. J.*, 2023, **461**, 142037.

[12] R. Andaveh, A.-S. Rouhaghdam, J.-P. Ai, M. Maleki, K. Wang, A. Seif, G.-B. Darband, J.-Y. Li, Boosting the electrocatalytic activity of NiSe by introducing MnCo as an efficient heterostructured electrocatalyst for large-current-density alkaline seawater splitting, *Appl. Catal. B-Environ.*, 2023, **325**, 122355.

[13] T.-T. Ma, X.-R. Shen, Q.-Z. Jiao, Y. Zhao, H.-S. Li, Y.-Y. Zhang, Y.-Z. Lv, C.-H. Feng, L. Guo, In-situ construction of hexagonal-star-shaped $MnCo_2S_4$@MoS_2 boosting overall water splitting performance at large-current-density: Compositional-electronic regulation, functions and mechanisms, *Chem. Eng. J.*, 2023, **464**, 142592.

[14] T. Zhang, J.-Y. Han, T.-M. Tang, J.-R. Sun, J.-Q. Guan, Binder-free bifunctional SnFe sulfide/oxyhydroxide heterostructure electrocatalysts for overall water splitting, *Int. J. Hydrogen Energy.*, 2023, **48**, 4594-4602.

[15] W.-W. Xu, T.-F. Ma, H.-C. Chen, D.-H. Pan, Z.-F. Wang, S.-X. Zhang, P. Zhang, S.-J. Bao, Q.-H. Yang, L.-H. Zhou, Z.-Q. Tian, S. Dai, Z.-Y. Lu, Scalable Fabrication of Cu_2S@NiS@Ni/NiMo Hybrid Cathode for High-Performance Seawater Electrolysis, *Adv. Funct. Mater.*, 2023, **33**, 2302263.

[16] P.-P. Tang, H. Wen, P. Wang, Hierarchically nanostructured Ni_2Fe_2N as an efficient electrocatalyst for hydrazine oxidation reaction, *Chem. Eng. J.*, 2022, **431**, 134123.

[17] T. Cui, J.-Q. Chi, J.-W. Zhu, X.-M. Sun, J.-P. Lai, Z.-J. Li, L. Wang, Tuning the size and chemisorption of FeP_4 by trace Ru doping for hydrazine-assisted hydrogen evolution in seawater at large-current-density, *Appl. Catal. B-Environ.*, 2022, 319, 121950.

[18] J.-F. Liu, H. Wen, Z.-Y. Zhang, P. Wang, An amorphous/nanocrystalline Ni_xP/Ni heterojunction for electrooxidation of hydrazine, *J. Mater. Chem. A*, 2023, **11**, 14213-14220.

[19] P. Shen, B.-W. Zhou, Z. Chen, W.-P. Xiao, Y.-L. Fu, J. Wan, Z.-X. Wu, L. Wang, Ruthenium-doped 3D Cu_2O nanochains as efficient electrocatalyst towards hydrogen evolution and hydrazine oxidation, *Appl. Catal. B-Environ.*, 2023, **325**, 122305.

[20] K. Li, Y. Tong, J.-F. He, X.-Y. Liu, P.-Z. Chen, Anion-modulated CoP electrode as bifunctional electrocatalyst for anion-exchange membrane hydrazine-assisted water electrolyser, *Mater. Horiz.*, 2023, **10**, 5277-5287.

[21] Q.-P. Yu, J.-Q. Chi, G.-S. Liu, X.-Y. Wang, X.-B. Liu, Z.-J. Li, Y. Deng, X.-P. Wang, L. Wang, Dual-strategy of hetero-engineering and cation doping to boost energy-saving hydrogen production via hydrazine-assisted seawater electroly, *Sci China Mater.*, 2022, **65**, 1539-1549.

[22] L.-L. Guo, Q.-P. Yu, X.-J. Zhai, J.-Q. Chi, T. Cui, Y. Zhang, J.-P. Lai, L. Wang, Reduction-induced interface reconstruction to fabricate $MoNi_4$-based hollow nanorods for hydrazine oxidation assisted energy-saving hydrogen production in seawater, *Nano Resv.*, 2022, **15**, 8846-8856.

[23] Q.-P. Yu, X.-B. Liu, G.-S. Liu, X.-P. Wang, Z.-J. Li, B. Li, Z.-X. Wu, L. Wang, Constructing Three-Phase Heterojunction with 1D/3D Hierarchical Structure as Efficient Trifunctional Electrocatalyst in Alkaline Seawater, *Adv. Funct. Mater.*, 2022, **32**, 2205767.

[24] X.-J. Zhai, Q.-P. Yu, J.-Q. Chi, X.-P. Wang, B. Li, B. Yang, Z.-J. Li, J.-P. Lai, L. Wang, Accelerated dehydrogenation kinetics through Ru, Fe dual-doped Ni_2P as

bifunctional electrocatalyst for hydrazine-assisted self-powered hydrogen generation, *Nano Energy*, 2023, **105**, 108008.

[25] W.-J. Liu, W.-X. Liu, T. Hou, J.-Y. Ding, Z.-G. Wang, R.-L. Yin, X.-Y. San, L.-G. Feng, J. Luo, X.-J. Liu, Coupling Co-Ni phosphides for energy-saving alkaline seawater splitting, *Nano Res.*, 2024, **17**, 4794-4806.

[26] X.-T. Wei, S.-C. Zhang, X.-S. Lv, S.-X. Dai, H.-L. Wang, M.-H. Huang, Local-reconstruction enables cobalt phosphide array with bifunctional hydrogen evolution and hydrazine oxidation, *Appl. Catal. B-Environ.*, 2024, **345**, 123661.

[27] Y.-F. Yang, X.-Y. Li, G.-L. Liu, H.-X. Liu, Y.-H. Shi, C.-M. Ye, Z. Fang, M.-X. Ye, J.-F. Shen, Hierarchical Ohmic Contact Interface Engineering for Efficient Hydrazine-Assisted Hydrogen Evolution Reaction, *Adv. Mater.*, 2024, **36**, 2307979.

[28] X.-Y. Wang, W.-H. Zhang, Q.-P. Yu, X.-B. Liu, Q.-C. Liang, X.-M. Meng, X.-P. Wang, L. Wang, Fe-doped CoNiP@N-doped carbon nanosheet arrays for hydrazine oxidation assisting energy-saving seawater splitting, *Chem. Eng. J.*, 2022, **446**, 136987.

[29] J.-Q. Chi, L.-L. Guo, J.-Y. Mao, T. Cui, J.-W. Zhu, Y.-A. Xia, J.-P. Lai, L. Wang, Modulation of Electron Structure and Dehydrogenation Kinetics of Nickel Phosphide for Hydrazine-Assisted Self-Powered Hydrogen Production in Seawater, *Adv. Funct. Mater.*, 2023, **33**, 2300625.

[30] W.-H. Zhang, X.-B. Liu, Q.-P. Yu, X.-Y. Wang, H.-M. Mao, J.-Q. Chi, B. Li, J. Wan, L. Wang, In situ electronic redistribution of Ni_2P hierarchical structure for energy-saving hydrogen production in seawater, *Chem. Eng. J.*, 2023, **454**, 140210.

[31] Y.-P. Ye, H.-Y. Li, J. Cao, X.-Y. Liu, H.-G. Fan, M.-B. Wei, L.-L. Yang, J.-H. Yang, Y.-L. Chen, Constructing microstructures in nickel-iron layered double hydroxide electrocatalysts by cobalt doping for efficient overall water splitting, *Int. J. Hydrogen Energy*, 2023, **48**, 17026-17034.

[32] Y.-A. Chang, X.-Y. Lu, S.-S. Wang, X.-X. Li, Z.-Y. Yuan, J.-C. Bao, Y. Liu, Built-In Electric Field Boosted Overall Water Electrolysis at Large Current Density for the Heterogeneous Ir/$CoMoO_4$ Nanosheet Arrays, *Small*, 2024, 2311763.

[33] T.-T. Ma, X.-R. Shen, Q.-Z. Jiao, Y. Zhao, H.-S. Li, Y.-Y. Zhang, Y.-Z. Lv, C.-H. Feng, L. Guo, In-situ construction of hexagonal-star-shaped $MnCo_2S_4$@MoS_2 boosting

overall water splitting performance at large-current-density: Compositional-electronic regulation, functions, and mechanisms, *Chem. Eng. J.*, 2023, **464**, 142592.

[34] Q.-N. Ha, N.-S. Gultom, C.-H. Yeh, D.-H. Kuo, One-pot synthesized Li, V co-doped Ni_3S_2 nanorod arrays as a bifunctional electrocatalyst for industrialization-facile hydrogen production via alkaline exchange membrane water electrolysis, *Chem. Eng. J.*, 2023, **472**, 144931.

[35] Y.-Y. Qian, B.-H. Zhou, Q. Zhang, H.-M. Yang, Rational Design of Goethite-Sulfide Nanowire Heterojunctions for High Current Density Water Splitting, *J. Phys. Chem. Lett.*, 2023, **14**, 6709-6718.

[36] S.-S. Li, E. Li, X.-W. An, X.-G. Hao, Z.-Q. Jiang, G.-Q. Guan, Transition metal-based catalysts for electrochemical water splitting at high current density: current status and perspectives, *Nanoscale*, 2021, **13**, 12788-12817.

[37] J.-L. Fan, C.-Y. Fu, R.-K. Liang, H.-Y. Lv, C.-S. Fang, Y.-H. Guo, W.-J. Hao, Mild Construction of "Midas Touch" Metal-Organic Framework-Based Catalytic Electrodes for Highly Efficient Overall Seawater Splitting, *Small*, 2022, **18**, 2203588.

[38] T.-Q. Yu, Q.-L. Xu, L. Luo, C.-R. Liu, S.-B. Yin, Interface engineering of NiO/RuO_2 heterojunction nano-sheets for robust overall water splitting at large current density, *Chem. Eng. J.*, 2022, **430**, 133117.